Electrochimica Acta 511 (2025) 145397

Contents lists available at ScienceDirect

Electrochimica Acta

journal homepage: www.journals.elsevier.com/electrochimica-acta

One-pot synthesis of heteroatom-rich anthraquinone-based benzoxazine-linked porous organic polymers for high performance supercapacitors

Ahmed F. Saber [a], Shimaa Abdelnaser [b], Ahmed F. M. EL-Mahdy [b,*], Shiao-Wei Kuo [b,*]

[a] Interdisciplinary Research Center for Hydrogen Technologies and Carbon Management (IRCHTCM), King Fahd University of Petroleum & Minerals, Dhahran 31261, Saudi Arabia
[b] Department of Materials and Optoelectronic Science, National Sun Yat-Sen University, Kaohsiung 80424, Taiwan

ARTICLE INFO

Keywords:
Porous organic polymers
Benzoxazine
Heteroatom-rich
Energy storage

ABSTRACT

Recently, the search for efficient and durable electrodes for energy storage has prompted the development of novel porous organic polymers (POPs). Here, we have studied the design, preparation and comprehensive characterization of a novel set of anthraquinone-based benzoxazine-linked POPs as electrode materials for supercapacitors (SCs). The polymers with high yield have been synthesized by direct coupling of various triamines, diphenol and paraformaldehyde. The benzoxazine linkage's formation and porosity parameters were readily analyzed using FTIR spectra, solid-state ^{13}C NMR and N_2 sorption analysis. The benzoxazine backbone provides the POPs with abundant nitrogen and oxygen heteroatoms, making them efficient candidates for storing energy. We observed that the superior benzoxazine-linked polymer exhibited the greatest electrochemical capacitance up to 117.7 F g^{-1} at 1.0 A g^{-1} was the An-TPA POP, which was mainly owing to the best microporous structure, accessible morphology and the largest specific surface area compared to others. In addition, it possessed the highest retention stability after 10,000 charge-discharge cycles (81.55 %), as well as lower ohmic resistance (5.38 Ω). Interestingly, a two-electrode system holding the An-TPA POP displayed an excellent electrochemical capacitance of 62 F g^{-1} at 1.0 A g^{-1}, a greater cycling retention of 95.71 % after 5000 GCD cycles at 10 A g^{-1}, as well as a prime energy density of 8.57 W h kg^{-1}. The results obtained demonstrated a significant tactic for constructing heteroatoms-rich POPs for next-generation SCs, offering improved efficiency and stability.

1. Introduction

Energy and environmental concerns are becoming increasingly prominent, drawing significant attention to the development and use of clean, renewable energy sources like wind and solar power [1,2]. However, the intermittent nature of these renewable energy sources greatly limits their exploration and widespread application. Maximizing the utilization of large-scale energy conversion and storage systems is a crucial technology for addressing this challenge [3–7]. In nature, renewable energy sources are sporadic, therefore, renewable energy systems must comprise an energy storage component [8]. Supercapacitors (SCs) are considered among the most favorable energy storage techniques that are extremely used today [9–12]. SCs are green energy storage devices between conventional capacitors and batteries, which have comprehensive characteristics over both [13–16]. They have a significantly higher power density than batteries, enabling rapid energy delivery and charging. At the same time, their energy density is several orders of magnitude greater than that of traditional capacitors, allowing them to store much more energy [17–19]. In addition, SCs are useful for many applications such as power supply, electric vehicles, aircraft, cranes, and emergency doors owing to their higher power density [20–22]. So, developing highly efficient electrode materials has a pivotal importance, to gain greater energy densities and effective energy conversion.

Electrode materials for SCs should be constructed with flexible and sturdy mechanical strength, because the systematic preparation of porous redox-active electrodes plays a substantial and favorable part in the improvement of high-performance SCs [23–25]. The electrode materials currently used are categorized into carbon-based materials [26,27], transition metal oxides [28,29], conductive polymeric materials,

* Corresponding authors.
E-mail addresses: ahmedelmahdy@mail.nsysu.edu.tw (A.F. M. EL-Mahdy), kuosw@faculty.nsysu.edu.tw (S.-W. Kuo).

https://doi.org/10.1016/j.electacta.2024.145397
Received 28 August 2024; Received in revised form 1 November 2024; Accepted 20 November 2024
Available online 21 November 2024

and organic polymeric materials [30]. Compared to metal oxides and conductive polymers, carbon-based electrodes offer several advantages including safety, wide availability, and facile preparation [31]. However, carbon materials are mostly in powder form, complicating the electrode manufacturing process [32–34]. On the other side, organic-based electrodes have gained increasing interest due to their outstanding features of high electrochemical efficiency, environmental friendliness, and easy preparation [35].

Porous organic polymers (POPs), including conjugated microporous polymers (CMPs), covalent organic frameworks (COFs), and hypercrosslinked polymers (HCPs), have been considered as hopeful materials offering large specific surface areas and porous characteristics. They have been utilized in various applications, such as energy storage, catalysis, pollutant removal and gas uptake/separation [36–43]. For instance, Jiang and Tan research groups demonstrated that POPs possessed a higher capacitance for carbon dioxide and iodine capture [44,45]. Wang et al. prepared a 3D-COF membrane for mono- and multivalent sieving of ions [46]. Pan's team have also synthesized a set of POPs holding dibenzothiophene-S,S-dioxide building block for hydrogen generation [47]. Additionally, Mai's group successfully constructed a porphyrin-based tube-like CMP featuring a large surface area for application in photocatalysis [48]. POPs in particular have emerged as outstanding electrode materials for SCs owing to their cheapness, great specific surface areas, tunable pore size, and high stability [49]. Diverse synthetic reactions (e.g., Yamamoto, Suzuki, Schiff base formation, and Friedel-Crafts coupling) have been applied to synthesize POPs with several linkages (e.g., imine, imide, boroxine, triazine, and hydrazine units) [50–56].

The heteroatom-rich POPs are a remarkable type of organic materials due to their high concern for energy storage and other applications. Nitrogen-rich polymers have substantial photoelectric characteristics that lead to more interest from all research groups [57]. For illustration, the existence of nitrogen heteroatoms within polymeric structure improves not only the conductivity, but also enhances wettability, and endows pseudocapacitance, resulting in greater electrochemical efficiency [58,59]. Benzoxazine-based derivatives (BZ) are a kind of motivating heteroatom-rich materials that can be constructed via the condensation chemical reaction of phenol, amine and formaldehyde, with the merits of excellent electronic, thermal, and mechanical characteristics and great stabilities as well [60–64]. The oxazine ring consists of nitrogen and oxygen heteroatoms that exist above and below it, with a deformed half chair conformation, leading to certain rigidity [65]. As a result, the BZ building unit can grant their derivatives with high degree of nitrogen and oxygen contents. Lately, several researchers have focused on the synthesis of polybenzoxazine-based porous materials through ring-opening thermal polymerization or synthesis of microporous carbons using polybenzoxazine starting material [66–69]. However, the direct use of BZ linkage for the synthesis of POPs has been achieved rarely [70].

Anthraquinones (An), also referred to as anthracenediones, are aromatic hydrocarbons with polycyclic planar structure representing a subclass of the quinone family. The core structure 9,10-anthracenedione ($C_{14}H_8O_2$) consists of three fused benzene rings with two carbonyl functional groups in the medium ring [71]. The variety of the An-based compounds depends on the nature and the location of the substituent groups that displace the hydrogen atoms on the main skeleton such as hydroxyl, methyl, methoxy, hydroxymethyl, formyl, carboxylic, or more complex substituents. The An-based derivatives have a wide spectrum of applications, in which they can be used as anticancer agents [72,73], antiplasmodial [74], antiviral agents [75], antibacterial agents [76], and anti-inflammatory agents [77]. In addition, cheap An-based derivatives have been applied as electroactive candidates in aqueous flow batteries [78].

In this context, we have reported for the first time a novel series of An-based BZ-linked POPs, which were constructed using various triamine monomers condensed directly in one step with paraformaldehyde and 1,5-dihydroxyanthracene-9,10-dione via Mannich reaction (Scheme 1). In contrast to the conventional BZ resins, that can be prepared through thermal polymerization and ring-opening reaction of BZ rings, the as-synthesized POPs in the outlined study consist of extended oxazine units with porous network polymeric structures [61,79]. The BZ-linked POPs which were named as An-TPA, An-TPP, and An-TPT, have been produced by polymerization reaction of 1,5-dihydroxyanthracene-9,10-dione and paraformaldehyde with tris(4-aminophenyl) amine, 2,4,6-tris(4-aminophenyl)pyridine, and 2,4,6-tris(4-aminophenyl)triazine, respectively. The An-TPA, An-TPP, and An-TPT POPs were obtained as insoluble solid materials in 85.35 %, 86.48 %, and 81.62 % yields, respectively. The porosity nature has been specified by nitrogen sorption isotherms, which confirmed the porous structure of polymers with pore sizes distributed mostly in the microporous range. The capability of the synthesized BZ-based POPs to be utilized as electrodes for SCs have been investigated by electrochemical measurements with a specific capacitance up to 117.7 F g^{-1} in three-electrode system, and 62 F g^{-1} in two-electrode system, which were among the best values for polymer-based electrodes.

2. Experimental section

2.1. Materials and characterizations

All solvents and chemicals were obtained from commercial suppliers and have been utilized as obtained unless otherwise noted. 1,5-Dihydroxyanthracene-9,10-dione (An-2OH), paraformaldehyde (HCHO), sodium hydroxide (NaOH) and acetic acid (AcOH) (99.8 %) were ordered from Sigma-Aldrich. Palladium on activated carbon (10 % Pd/C) as well as *p*-nitrobenzaldehyde (99 %) were ordered from Acros. *p*-Nitroaniline (99 %) was acquired from Fluka. Ammonium acetate (NH_{4OAc}) (97 %) was obtained from Showa. Whereas *p*-nitroacetophenone (98 %), hydrazine hydrate ($NH_2NH_2.H_2O$) (≥ 98 %), *p*-fluoronitrobenzene (99 %), trifluoromethanesulfonic Acid (≥ 98 %), potassium carbonate (K_2CO_3, 99.9 %), chloroform ($CHCl_3$) and methanol (MeOH) were obtained from Alfa Aesar. 1,4-Dioxane and dimethyl sulfoxide (DMSO) were purchased from J. T. Baker. *p*-Aminobenzonitrile (98 %) was purchased from Matrix scientific. Ethanol (EtOH) was purchased from Kelong Chemistry Reagent. All characterizations of the constructed BZ-linked polymers have been shown in Supporting Information (ESI).

2.2. Preparation of POPs

In brief, a solution of 3.3 mmol of the utilized triamines (TPA-3NH_2, TPP-3NH_2, TPT-3NH_2) in dioxane was gradually added to a suspension of 40 mmol HCHO in dioxane with two drops of 1 M NaOH at 5–10 °C. The resulting suspension was stirred for 2 h before 10 mmol of An-2OH in dioxane was added. Then the mixture was stirred at 80 °C for an additional 8 h. The produced solid was filtered and washed several times to yield the corresponding An-based POPs. Eventually, the produced solid materials were dried at 100 °C for 10 h. The complete synthetic procedures have been shown in Supporting information (ESI).

3. Results and discussion

3.1. Structural design, preparation, and characterizations

Firstly, we have utilized Fourier transform infrared (FTIR) spectra to characterize the BZ linkage's formation for all the polymers (Fig. 1A). For the An-TPA POP, the vibrational peaks at 1231 and 1087 cm^{-1} were attributed to the existence of the aromatic ether oxazine unit, owing to the asymmetric and symmetric C—O-C vibrational modes, respectively [80]. The An-TPP POP exhibited the corresponding peaks at 1236 and 1076 cm^{-1}, respectively, whereas the observed peaks for the An-TPT POP were centered at 1241 and 1070 cm^{-1}, respectively. In

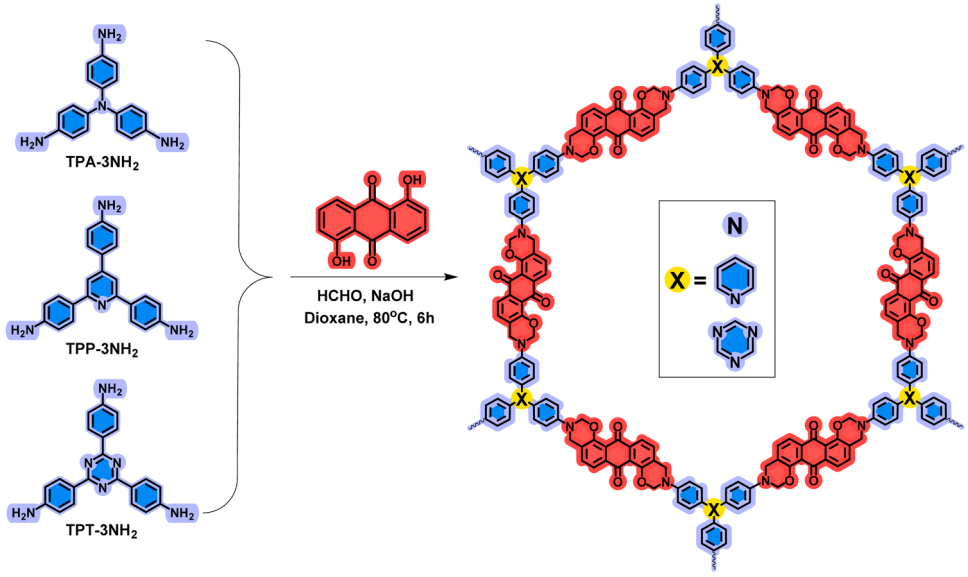

Scheme 1. Synthesis of (a) An-TPA, (b) An-TPP and (c) An-TPT POPs.

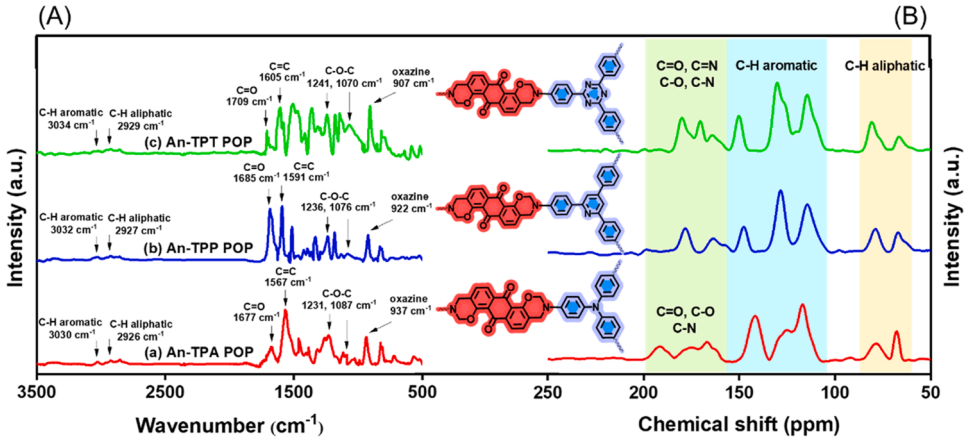

Fig. 1. (A) FTIR spectra; (B) solid state ^{13}C NMR spectra of An-TPA, An-TPP and An-TPT polymers.

particular, the absorption bands at 907, 922 and 937 cm^{-1} are ascribed to stretching vibrations of benzene rings that directly linked to the oxazine units for An-TPA, An-TPP and An-TPT POPs, respectively. Also, the absorption bands assigned to C=O stretching vibrations of An units were located at 1709, 1685 and 1677 cm^{-1} corresponding to the An-TPA, An-TPP and An-TPT polymers, respectively. Moreover, the stretching vibration absorption peaks assigned to C—H aliphatic and C—H aromatic functional groups for the An-TPA polymer were 2929 and 3034 cm^{-1}, respectively, for the An-TPP polymer were 2927 and 3032 cm^{-1}, respectively, and for the An-TPT polymer were 2926 and 3030 cm^{-1}, respectively. Additional investigation into the structural composition of the prepared BZ-linked POPs was conducted using solid-state ^{13}C nuclear magnetic resonance (NMR) spectra. In the obtained spectra of the An-TPA, An-TPP and An-TPT polymers, three various modes of resonance peaks have been obviously noticed. The intense signals in the range of 100–155 ppm are characteristic of aromatic carbon atoms. The observed signals in the range 58–86 ppm are related to the methylene carbons directly connected to oxygen and nitrogen atoms, as a logic proof for the presence of oxazine ring. In addition, the small peaks within the range (155–200 ppm) are assigned to C=O, C—O and C—N carbon nuclei of the An-TPA POP, and are also characteristic of the C=O, C=N, C—O and C—N carbons of both the An-TPP and An-TPT polymers (Fig. 1B).

The thermal gravimetric analysis (TGA) showed that the POPs under study possessed considerable degree of thermal stabilities. One can observe that the An-TPP and An-TPT polymers had the highest thermal stabilities with values of 400 °C and 434 °C, respectively, which are slightly greater than that of the An-TPA POP (348 °C). Besides that, TGA analysis provided that the char yield values for the An-TPA and An-TPT polymers were estimated to be 39 % and 35 %, respectively, whereas the top value was recorded as 42 % corresponding to the An-TPP polymer. From the above-mentioned results, it can be concluded that our porous polymers are thermally stable (Fig. S15 and Table S1).

XRD measurements for the as-prepared BZ-linked polymers demonstrated no observed diffraction peaks which emphasize their amorphous nature (Fig. S16), as reported for other polymers [81,82].

3.2. Porosity and morphology

The porosity measurements have been carried out using N_2 sorption at 77 K. The resultant curves revealed type II isotherms which are featured for microporous structure. The An-TPA polymer had the highest Brunauer-Emmett-Teller specific surface area (S_{BET}) up to 26.51 $m^2\ g^{-1}$ among the series, whereas the An-TPP and An-TPT POPs possessed the S_{BET} of 18.52 $m^2\ g^{-1}$ and 9.00 $m^2\ g^{-1}$, respectively (Fig. 2a). The pore size distributions of the as-prepared BZ-linked

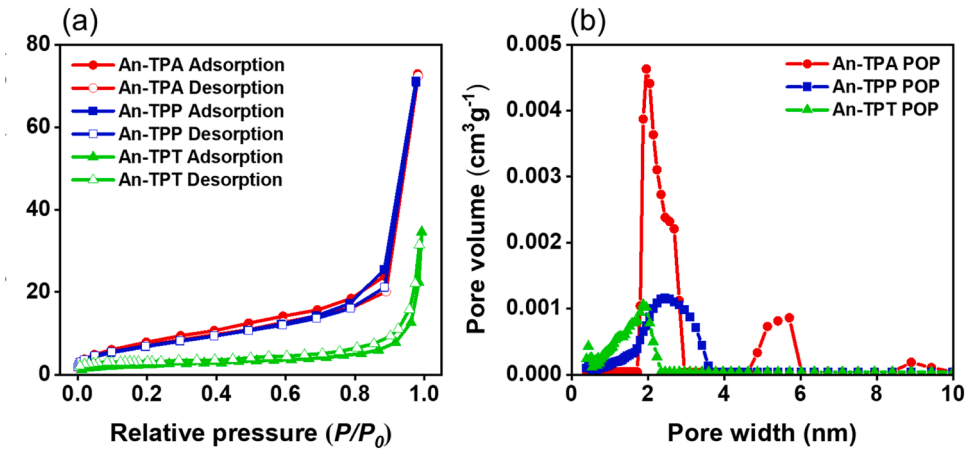

Fig. 2. Nitrogen sorption curves of (a) An-TPA, An-TPP and An-TPT polymers. The pore size distribution profiles of (b) An-TPA, An-TPP and An-TPT POPs.

polymers were also estimated based on a non-local density functional theory (NLDFT). The pore sizes observed were basically distributed in microporous and mesoporous ranges, in accordance with the isothermal curves. The An-TPA polymer displayed one micropore with a pore width of 1.96 nm in addition to one mesopore at 5.71 nm. For the An-TPP, there is only one mesopore at 2.45 nm, while a micropore at 1.88 nm was observed for the An-TPT polymer. Furthermore, the total pore volume for the polymers have been determined to be 0.005, 0.001 and 0.001 $cm^3\ g^{-1}$ corresponding to the An-TPA, An-TPP and An-TPT POPs, respectively. Both the An-TPP and An-TPT polymers represented a smaller S_{BET} in comparison to the An-TPA POP, which can be explained in terms of their highly packed structure due to the presence of planar pyridine and triazine rings, respectively (Fig. 2b and Table S2).

The structural morphologies of our novel polymers have been probed by both field emission scanning electron microscope (FE-SEM) as well as the high-resolution transmission electron microscope (HR-TEM). The SEM photos represented the polymers as accumulated microgel particles with sizes ranged from 1 to 2 μm scale. The An-TPA POP was displayed as plate like morphology, while either the An-TPP or An-TPT polymers showed spherical like morphologies (Fig. 3a–c). The elemental mapping resulted from the energy dispersive X-ray spectroscopy (EDS) revealed the existence of carbon, nitrogen and oxygen atoms with symmetrical distribution on the surface of all polymers (Fig. S17). The HR-TEM photos showed the amorphous porous texture for all polymers (Fig. 3d–f).

3.3. Electrochemical measurements

Focusing on polymeric organic materials as efficient candidates for sustainable energy storage, we have studied the potential of our synthesized BZ-linked polymers as electrode materials for SCs. The cyclic voltammetry (CV) studies of the obtained polymers have been carried out using a three-electrode system with KOH electrolyte (1.0 M) over a specific potential range of −1.0 to 0 V. The CV curves obtained, showed semi-rectangular shapes with small peculiar humps within the applied potential window (Fig. 4a-c). By increasing the scan rate potential, there is also an observed increase in the CV's peak current of our BZ-linked electrodes, demonstrating that their electrochemical capacitance is influenced by both pseudocapacitance and electric double-layer capacitance (EDLC) with minimum charge transfer resistance [83]. The reason of such humps in the CV curves was mainly the presence of nitrogen and oxygen heteroatoms as well as electron-rich benzene rings, which can also improve the pseudocapacitance (Figs. S18–S20).

For all the synthesized An-based POPs, galvanostatic

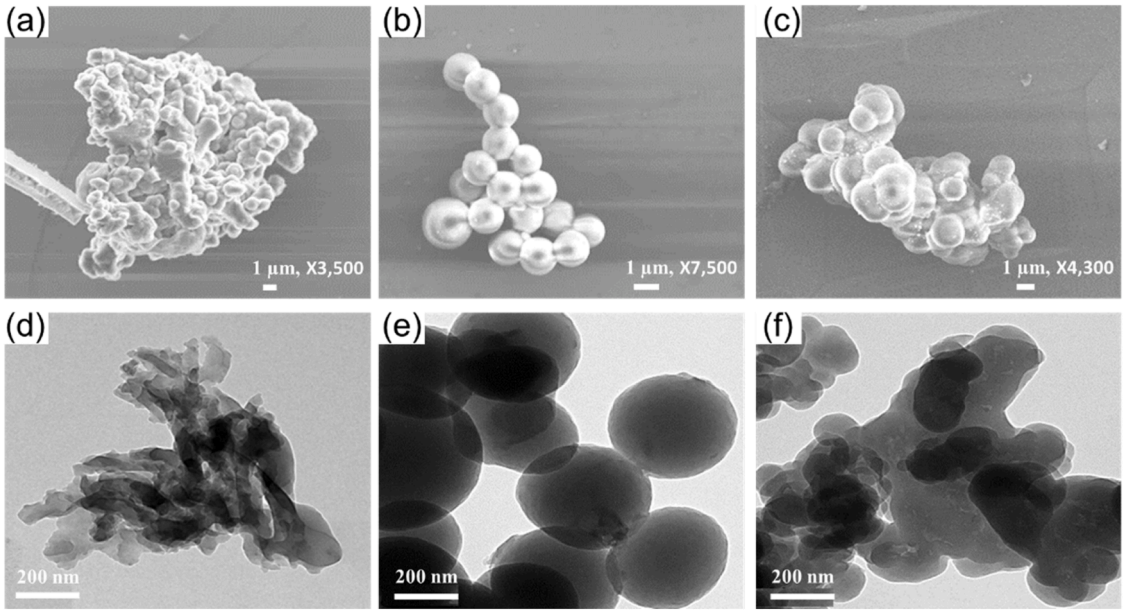

Fig. 3. SEM photos of (a) An-TPA, (b) An-TPP and (c) An-TPT POPs. TEM photos of (d) An-TPA, (e) An-TPP and (f) An-TPT.

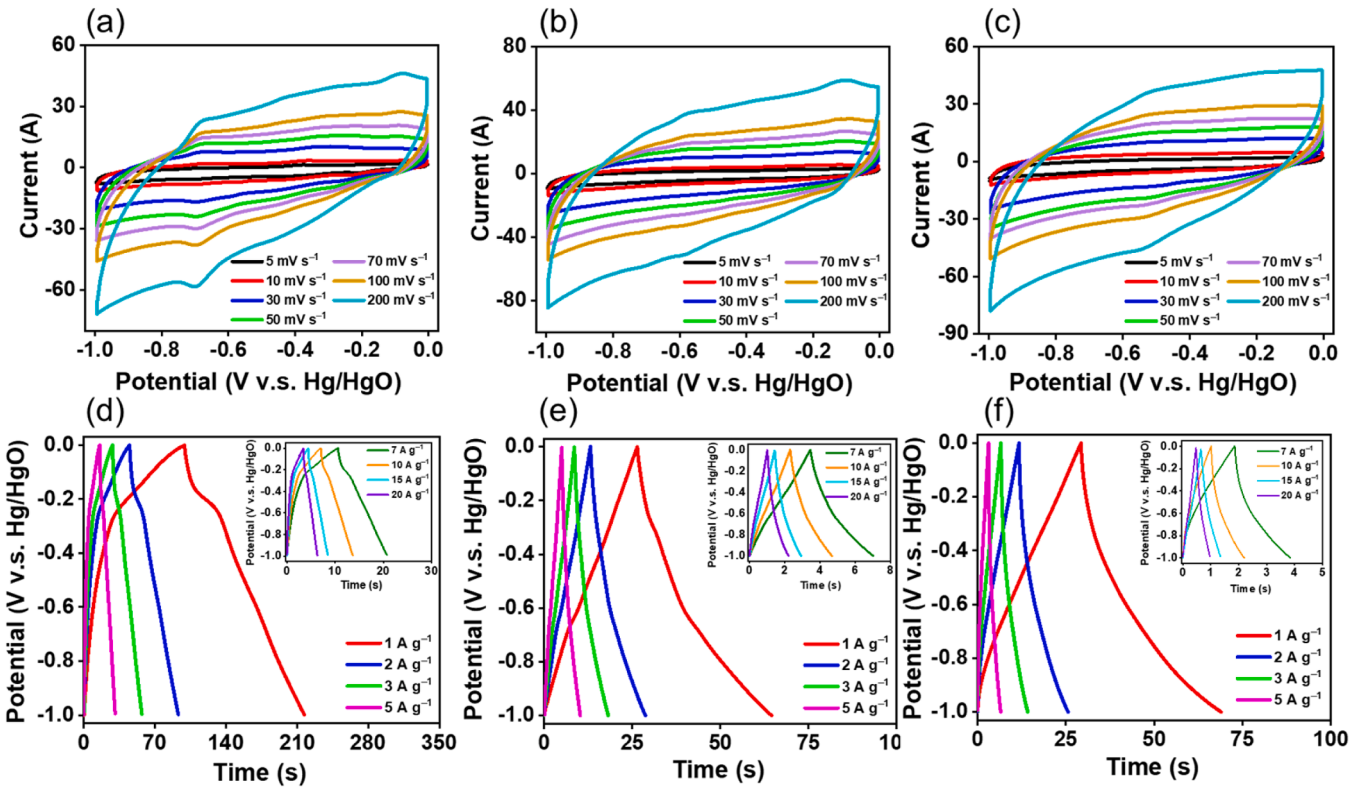

Fig. 4. CV curves of (a) An-TPA, (b) An-TPP and (c) An-TPT polymers. The corresponding GCD curves of (d) An-TPA, (e) An-TPP and (f) An-TPT polymers, recorded at various current densities in the three-electrode system.

charge−discharge (GCD) has been investigated in the range from 1.0 to 20 A g^{-1} (Fig. 4d-F). A typical triangular shape with trivial deviation was observed in the GCD curves, confirming both EDLC and pseudocapacitance types of capacitances, in full agreement with the results obtained from the CV measurements. GCD analysis displayed specific capacitances for An-TPA POP to be 117.7, 95.64, 86.28, 76.6, 71.82, and 66.2 Fg^{-1} at specific current densities of 1, 2, 3, 5, 7, and 10 A g^{-1}, aligning with the CV's findings. At 1.0 A g^{-1} current density, the greater electrochemical capacitance of An-TPA POP, nearly 3 times of those of the An-TPP POP (38.12 Fg^{-1}) and the An-TPT POP (39.63 F g^{-1}), is mainly because of slower diffusion rate of KOH ions into the polymer's sunken pores as well as their inability to reach the electrode's surface at higher current densities (Fig. 5a). Then, by increasing the current density, the ion motion is dramatically reduced, resulting in a significant reduction in specific capacitance. Moreover, Table S3 compares the efficiency of our BZ-linked POPs with other polymers previously reported. For example, Mei group prepared the MPc-CMPs and then hybridized them with CNTs by vacuum filtration. The GCD analysis at 1.0 A g^{-1} represented that the capacitance of CoPc-CMP is 13.8 F g^{-1} in 1 M H_2SO_4 [84]. Also, Khattak et al. prepared DAB-TFP COF and applied it as electrode material for SCs. The electrochemical capacitance was measured to be 98 F g^{-1} at 0.5 A g^{-1} [85]. Moreover, the TBN-Py and TBN—Car polymers possessed electrochemical capacities of 31 and 18.9 F g^{-1} at 0.5 A g^{-1} [86]. However, the as-prepared An-based POPs exceeded other electrode materials in terms of electrochemical performance. Its synthetic route is also simple, cheap, and scalable for further research.

The specific capacitance C_s (F g^{-1}) can be calculated from GCD curves by applying the relationship (1).

$$C_s = \frac{1 \times \Delta t}{m \times \Delta V} \tag{1}$$

where, I/m (A g^{-1}) refers to the utilized current density, Δt (s) refers to the discharging time, ΔV (V) refers to the applied potential.

In case of resemblance to battery type behavior, the specific capacity Q_s (C g^{-1}) can be calculated by utilizing the relationship (2).

$$Q_s = \frac{1 \times \Delta t}{m} \tag{2}$$

In addition, the applied potential window in the three-electrode system for our polymeric electrodes was 1.0 V, so, the specific capacitance and the specific capacity are the same and we can use either of their units [87].

Batteries and SCs differ in their charge-storage properties due to their electrochemical processes. In lithium-ion batteries, the movement of lithium ions, which enables redox processes within bulk electrode materials, is governed by diffusion and can be relatively slow. On the other hand, SCs store energy by adsorption of electrolyte ions on the electrode's surface. There are no redox reactions required, so the response to potential's changes without diffusion limitations is fast and gives a great power. However, the energy density of SCs is smaller than that of batteries because the charge is confined to the surface. SCs can be recognized from batteries using potentiostatic and galvanostatic techniques. To clarify, SCs are characterized by rectangular CV curves and a linear time-dependent change in potential at a fixed current. Whereas, in batteries, the CV curves are distinguished by faradaic redox peaks with wide voltage separation between them [88,89].

The cyclic stability measurements are more important for the evaluation of electrode's Coulombic efficacy and capacitive retention. Fig. 5b and Fig. S21 represent the cycling stability of the An-based POP electrodes, maintaining 81.55, 78.52, and 75.05 % of their original capacitance, respectively, over 10,000 GCD cycles. As illustrated in Fig. 5c,d, further electrochemical measurements of the electrode's nature are also crucial. The Nyquist plot represented the resistance spectrum with a straight line at both higher and lower frequency regions. The first intersection of this plot with the X-axis demonstrates the resistance of solutions, including the intrinsic electrode resistance, the

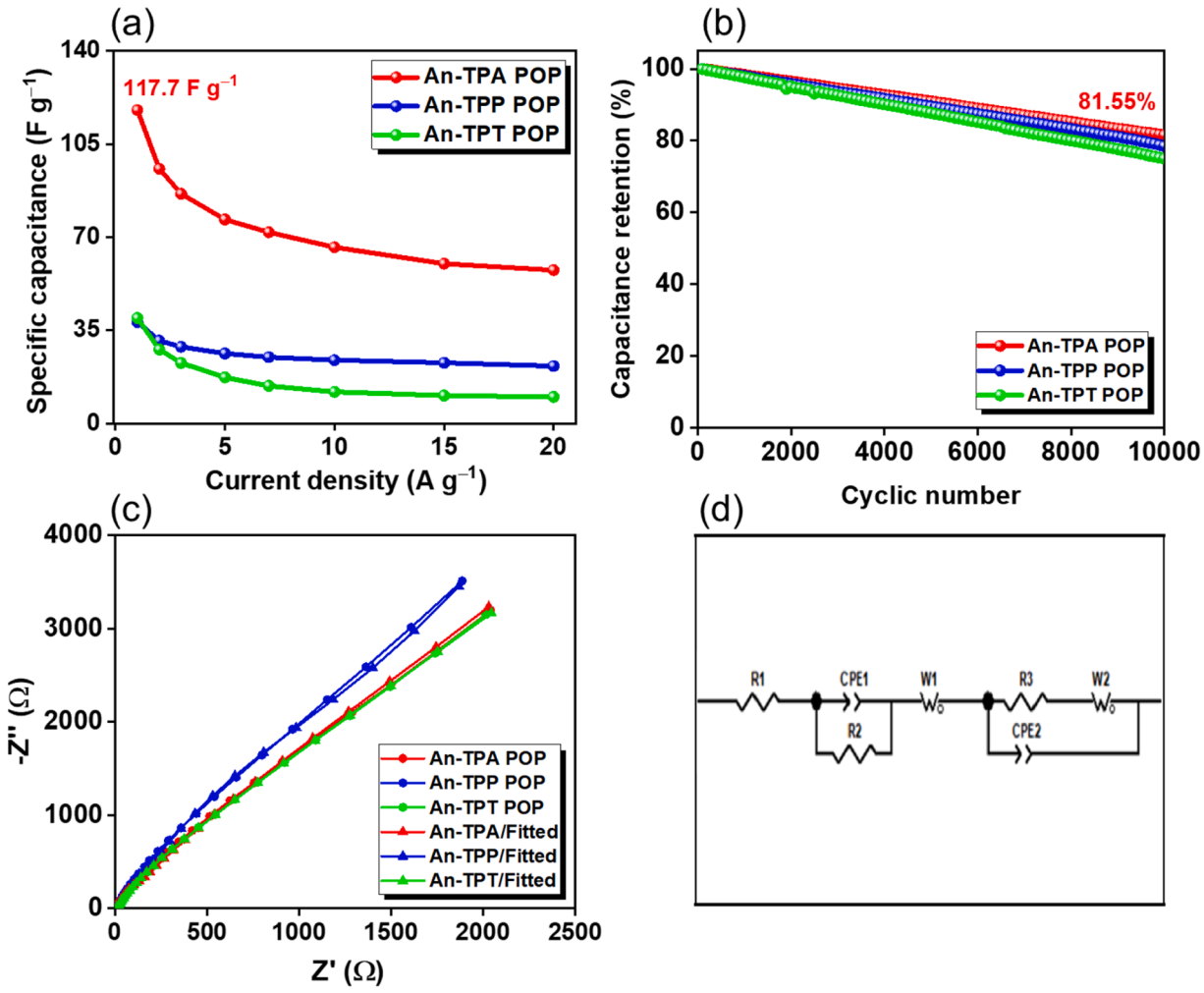

Fig. 5. (a) GCD electrochemical capacitances of An-TPA, An-TPP and An-TPT POPs measured at different current densities (1.0 to 20 A g^{-1}). (b) Cycling stability of the polymeric electrodes, measured at a current density of 10 A g^{-1} over 10,000 cycles. (c) Nyquist plots of three-electrode system for POPs before and after fitting. (d) Equivalent fitting circuit.

ionic KOH resistance, the interior impedance of the electrode, and the interfacial impedance on the electrode/electrolyte interface. The slope in the small frequency region of the Nyquist curve is signalized of diffusion Warburg resistance, that describes the diffusion of KOH ions as well as electrons through the electrode, confirming easy transfer. The Nyquist plots and their fitting showed the resistance of the An-TPA, An-TPP, and An-TPT POPs to be 5.38, 3.94, and 7.45 Ω, respectively, showing smaller resistance and delivering greater electrochemical capacitance of our polymeric electrodes. The excellent capacitive behavior of our POPs was extra confirmed using the frequency-dependent magnitude Bode plots which demonstrated negative slope lines at lower frequencies, and very small resistance at higher frequency range (Fig. S22a). The knee frequency at 45° phase angle (equal capacitance and resistance properties) were estimated using frequency-dependent phase-angle Bode plots for the as-prepared polymers. The calculated knee frequencies for the An-TPA, An-TPP, and An-TPT POPs were estimated to be 21.26, 57.21, and 83.97 Hz, respectively, suggesting their great performance for energy storage applications (Fig. S22b).

By using the power law Eq. (3), we have studied the correlation between current (i) and scanning rate (v) to learn deeply about the capacitive contribution of the synthesized polymers [90,91].

$$i = av^b \tag{3}$$

The b factor was calculated by plotting log (i) versus log (v), where a, b, and v are constants. Diffusion-controlled processes have a value of 0.5, while capacitive processes have a value of 1.0 for b. The calculated b values for the cathodic and anodic peaks of the An-TPA polymer were 0.64 and 1.34, respectively, while the b values for the An-TPP POP were 0.67 and 0.89, respectively, and for the An-TPT POP were 0.85 and 0.94, respectively (Fig. 6a–c). These results indicate that the energy storage of the polymers can be attributed to a combination of diffusion-controlled and capacitive processes occurring simultaneously [92]. The An-TPT polymer exhibited superior rate capacity compared to others, primarily due to its higher capacitive contribution, which can be attributed to its greater nitrogen content.

The capacitive and diffusion contributions to the total capacity were quantified using the following equation: [90,91]

$$i(V) = k_1 v + k_2 v^{1/2} \tag{4}$$

where i(V) is the overall current at a specific potential V and k_1v and $k_2v^{1/2}$ are the currents generated by the diffusion-controlled and capacitive effects, respectively. The capacitive contributions of the An-TPA, An-TPP and An-TPT POPs were 12 %, 16 % and 72 % at 5 mV s^{-1} of the total capacity, respectively. This confirms that the An-TPT POP exhibits a higher capacitive contribution than the other two polymers under study. By increasing the scan rate from 5 mV s^{-1} to 200 mV s^{-1}, the capacitive contribution also rose, reaching values of 47 % for the An-TPA polymer, 55 % for the An-TPP polymer and 94 % for the An-TPT

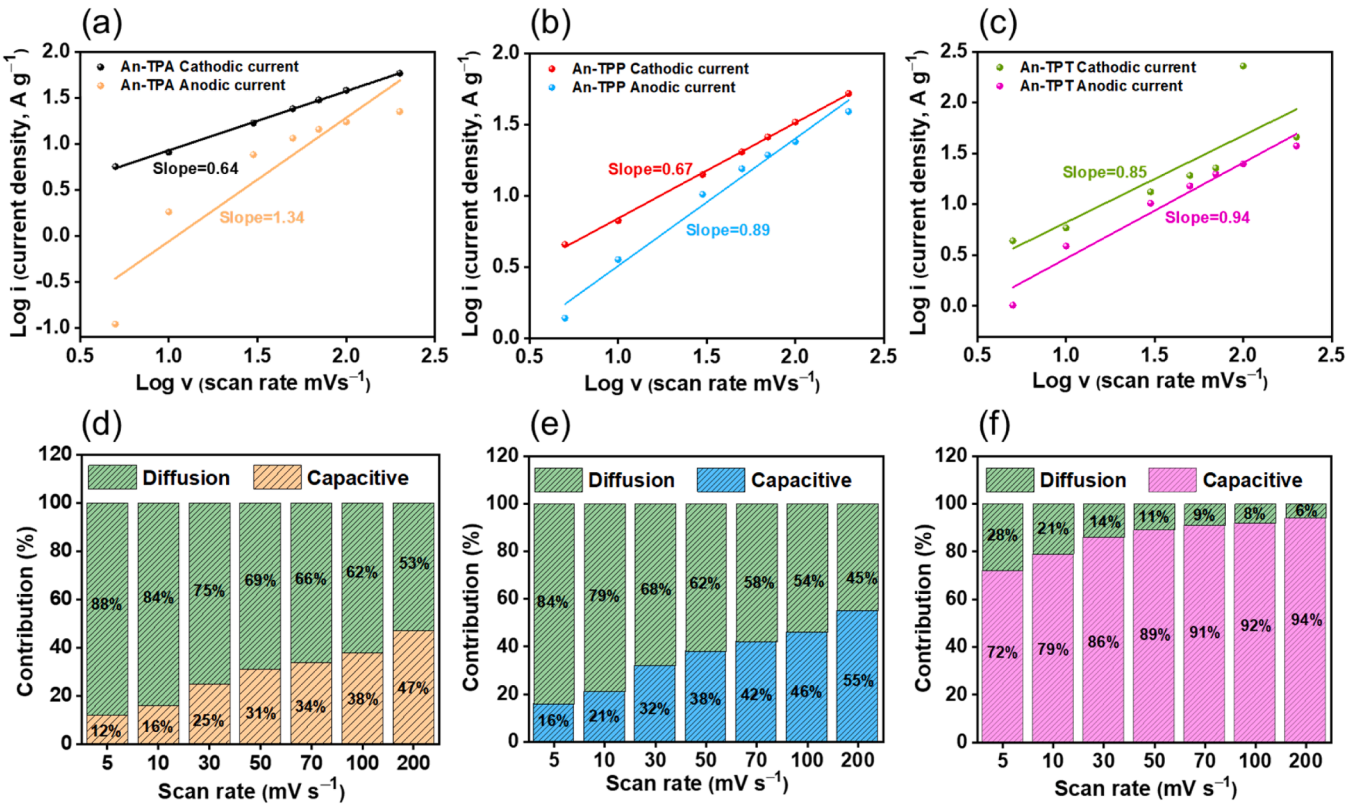

Fig. 6. (a-c) Log (i) versus Log (v) plots of (a) An-TPA, (b) An-TPP, and (c) An-TPT POPs. (d-f) The relative contribution of the capacitive and diffusion-controlled energy storage of (d) An-TPA, (e) An-TPP, and (f) An-TPT POPs, recorded at various scan rates.

polymer (Fig. 6d–F). The relative contributions of capacitive and diffusion currents of polymers recorded at 5 mV were shown in Fig. S23.

To evaluate the feasibility of using the An-TPA polymer as a device, we have tested its electrochemical performance within symmetric SCs (CR2032) in which our POP acts as both cathode and anode as well. The CV curves were measured at various scan rates from 5 to 200 mV s^{-1} (Fig. 7a), and GCD profiles at various current densities (1.0 − 10 A g^{-1}) with almost all CV curves had rectangular shapes (Fig. 7b).

The GCD profiles of the An-TPA POP showing an almost triangular shape with minimal curvature during discharge. This shape confirms both pseudocapacitive and EDLC behavior, aligning with the characteristics observed in the three-electrode system. The GCD discharge time was notably longer than the corresponding charge time, highlighting its suitability for practical applications. Moreover, after operation at specified current densities (1, 2, and 3 A g^{-1}), the coin device holding the An-TPA polymer demonstrated electrochemical capacitances of 62, 46.86, and 45 F g^{-1}, respectively (Fig. 7c). According to Ragone plot in Fig. 7d, at a value of 500 W kg^{-1} power density, the An-TPA polymer achieved excellent energy density value of 8.57 W h kg^{-1}, which was a comparative value to other porous materials (Table S4). The stability measurement for our synthesized redox-active An-TPA polymer over 5000 cycles at constant current density (10 A g^{-1}) was tested, the long-term cycling stability was confirmed by providing capacity retentions of 95.71 % (Fig. S24a). In addition, the Nyquist plots and the equivalent electric circuit of the An-TPA POP revealed that the internal resistance offered by its SSCs was 4.05 Ω, proving lower resistance and higher conductivity of this polymer (Fig. S24b,c). This value suggests that the polymer possesses high electrical conductivity and can be ideal source as electrode material for energy storage applications.

Furthermore, the frequency-dependent magnitude Bode plots have been applied to determine the resistance behavior, and the frequency-dependent phase-angle Bode plots have been studied to investigate the knee frequencies for the An-TPA POP. As shown in Fig. S25, this polymer exhibited negative slope's line at lower frequencies, minimum resistance at higher frequency range, and the estimated knee frequency at 45° phase angle was 58.78 Hz.

A key factor affecting the performance of SCs using inorganic electrolytes is their wettability [93]. When wettability is enhanced, ion transfer is facilitated, charge transfer is improved, and internal resistance is diminished. As a result, electrodes can achieve great capacities and have a longer cycle life [94]. Small contact angles (below 90°) allow the liquid to spread effectively on solid surfaces, suggesting relatively great wettability [95]. In addition, the presence of oxygen-containing functionalities significantly enhances the adsorption ability of electrode towards other materials, preventing the electrode from dissolving in the electrolyte and ensuring stable connection between the two materials during long-term cycling [96].

The hydrophilicity of the as-prepared polymers was compared with each other via water contact angle measurements (Fig. S26). As a result of higher heteroatoms content in the An-TPA, An-TPP, and An-TPT polymers, their contact angles were measured to be 47.7°, 74.1°, and 60.7°, respectively, confirming their increased hydrophilicities. The An-TPA POP with the top hydrophilicity possessed the best wettability, thus providing the highest electrochemical capacitance [95]. It is reported that the hydrophilicity is directly proportional to the heteroatoms' contents within the polymer, however, the An-TPA POP with the lowest contents of heteroatoms displayed the highest hydrophilicity [51]. This can be explained in terms of increased planarity of TPP and TPT units which leads to higher pi-pi stacking and greater shielding effect of their heteroatoms, but in case of TPA unit, which is not planar, it gives rise to lower pi-pi stacking and smaller shielding effect. In addition, the An-TPT polymer possessed higher hydrophilicity compared to the An-TPP polymer owing to its higher nitrogen content.

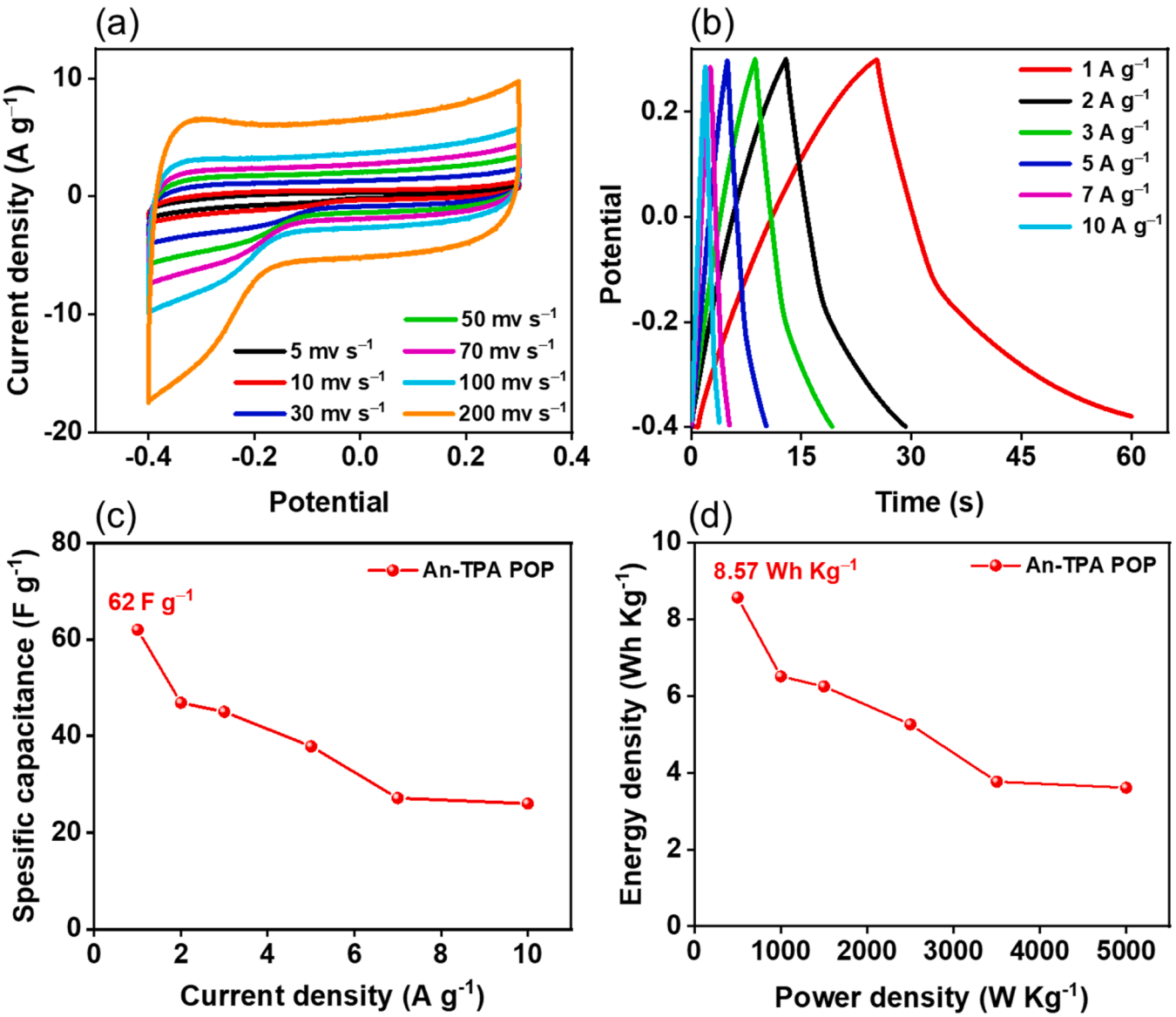

Fig. 7. (a) CV curves; (b) GCD curves; (c) GCD specific capacitances recorded at current densities from 1.0 to 10 A g^{-1}; (d) Ragone plots in two-electrode system for the An-TPA polymer.

4. Conclusions

To conclude, three robust BZ-linked POPs have been successfully developed through the Mannish coupling reaction of triamino-derivatives with 1,5-dihydroxyanthracene-9,10-dione in the presence of paraformaldehyde. The produced polymers demonstrated a high degree of thermal stability with the maximum T_{d10} value of 434 °C and the top char yield value up to 42 %. The heteroatom enriched POPs were confirmed to be efficient electrodes for SCs with an electrochemical capacitance value of 117.7 F g^{-1} (measured at 1.0 A g^{-1}), and an impressive retention stability of 81.55 % after 10,000 cycles (measured at 10 A g^{-1}) in three-electrode system. Furthermore, a two-electrode system holding An-TPA polymer displayed a good capacitance (62 F g^{-1}) at 1.0 A g^{-1}, a high stability retention (95.71 %) over 5000 cycles at 10 A g^{-1}, and an outstanding energy density (8.57 W h kg^{-1}) at 500 W kg^{-1} power density. The present work could pave a new synthetic tool for exploring novel approaches in preparing heteroatom-rich POPs as promising candidates for energy storage.

CRediT authorship contribution statement

Ahmed F. Saber: Writing – original draft, Methodology, Investigation, Formal analysis, Data curation, Conceptualization. **Shimaa Abdelnaser:** Formal analysis, Data curation. **Ahmed F. M. EL-Mahdy:** Writing – review & editing, Supervision. **Shiao-Wei Kuo:** Writing – review & editing, Supervision, Project administration, Funding acquisition.

Declaration of competing interest

The authors declare the following financial interests/personal relationships which may be considered as potential competing interests: Ahmed Fathi Saber reports equipment, drugs, or supplies was provided by National Sun Yat-sen University. Ahmed Fathi Saber reports equipment, drugs, or supplies was provided by King Fahd University of Petroleum & Minerals. If there are other authors, they declare that they have no known competing financial interests or personal relationships that could have appeared to influence the work reported in this paper.

Acknowledgment

This study was supported financially by the Ministry of Science and Technology, Taiwan, under contracts NSTC112–2218-E-110–007 and 112–2223-E-110–002.

Supplementary materials

Supplementary material associated with this article can be found, in the online version, at doi:10.1016/j.electacta.2024.145397.

Data availability

Data will be made available on request.

References

[1] P. Wang, X. Shi, Z. Wu, S. Guo, J. Zhou, S. Liang, Layered hydrated vanadium oxide as highly reversible intercalation cathode for aqueous Zn-ion batteries, Carbon Energy 2 (2020) 294–301, https://doi.org/10.1002/cey2.39.
[2] Q. Liu, H. Zhang, J. Xie, X. Liu, X. Lu, Recent progress and challenges of carbon materials for Zn-ion hybrid supercapacitors, Carbon Energy 2 (2020) 521–539, https://doi.org/10.1002/cey2.69.
[3] W. Raza, F. Ali, N. Raza, Y. Luo, K.H. Kim, J. Yang, S. Kumar, A. Mehmood, E. E. Kwon, Recent advancements in supercapacitor technology, Nano Energy 52 (2018) 441–473, https://doi.org/10.1016/j.nanoen.2018.08.013.
[4] N. Devillers, S. Jemei, M.C. Péra, D. Bienaimé, F. Gustin, Review of characterization methods for supercapacitor modelling, J. Power Sources 246 (2014) 596–608, https://doi.org/10.1016/j.jpowsour.2013.07.116.
[5] L. Zhang, X. Hu, Z. Wang, F. Sun, D.G. Dorrell, A review of supercapacitor modeling, estimation, and applications: a control/management perspective, Renew. Sust. Energy Rev. 81 (2018) 1868–1878, https://doi.org/10.1016/j.rser.2017.05.283.
[6] L. Zhou, J. Zhang, Y. Wu, W. Wang, H. Ming, Q. Sun, L. Wang, J. Ming, H. N. Alshareef, Understanding ostwald ripening and surface charging effects in solvothermally-prepared metal oxide-carbon anodes for high performance rechargeable batteries, Adv. Energy Mater. 9 (43) (2019) 1902194, https://doi.org/10.1002/aenm.201902194.
[7] Q. Zhang, Y. He, Y. Wang, J. Lu, N. Jiang, Y. Yang, Rational integration of carbon nanotubes into chain-engineered bipolar polyimides as core-shell heterostructured electrodes for polymer-based symmetrical full batteries, Adv. Funct. Mater. 33 (5) (2023) 2211590, https://doi.org/10.1002/adfm.202211590.
[8] Z. Yang, J. Zhang, M.C. Kintner-Meyer, X. Lu, D. Choi, J.P. Lemmon, J. Liu, Electrochemical energy storage for green grid, Chem. Rev. 111 (2011) 3577–3613, https://doi.org/10.1021/cr100290v.
[9] P. Krishnaiah, B.P. Prasanna, K.Y. Kumar, P.K. Asha, N. Piyushi, V.S.A. Devi, F. A. Alharthi, M.S. Raghu, Fabrication of anode material for asymmetric supercapacitor device using polyaniline wrapped boroncarbonitride nanocomposite with enhanced capacitance, J. Alloy. Comp. 848 (2020) 156602, https://doi.org/10.1016/j.jallcom.2020.156602.
[10] S.B. Alahakoon, C.M. Thompson, G. Occhialini, R.A. Smaldone, Design principles for covalent organic frameworks in energy storage applications, ChemSusChem 10 (2017) 2116–2129, https://doi.org/10.1002/cssc.201700120.
[11] T. Zhang, C. Li, F. Wang, A. Noori, M.F. Mousavi, X. Xia, Y. Zhang, Recent advances in carbon anodes for sodium-ion batteries, Chem. Rec. 22 (2022) e202200083, https://doi.org/10.1002/tcr.202200083.
[12] C. Li, C. Zheng, F. Cao, Y. Zhang, X. Xia, The development trend of graphene derivatives, J. Electron. Mater. 51 (2022) 4107–4114, https://doi.org/10.1007/s11664-022-09687-4.
[13] X. He, T. Zhuang, S. Ruan, X. Xia, Y. Xia, J. Zhang, H. Huang, Y. Gan, W. Zhang, An innovative poly(ionic liquid) hydrogel-based anti-freezing electrolyte with high conductivity for supercapacitor, Chem. Eng. J. 466 (2023) 143209, https://doi.org/10.1016/j.cej.2023.143209.
[14] X. He, W. Li, Y. Xia, H. Huang, X. Xia, Y. Gan, J. Zhang, W. Zhang, Pivotal factors of wood-derived electrode for supercapacitor: component striping, specific surface area and functional group at surface, Carbon N Y 210 (2023) 118090, https://doi.org/10.1016/j.carbon.2023.118090.
[15] Y. Dou, H. Li, Y. Dong, X. Zhang, K. Chen, Y. Yang, Macromolecular engineering of polyquinone-based electrode materials for high-energy supercapacitors, ACS Appl. Energy Mater. 5 (1) (2022) 1331–1340, https://doi.org/10.1021/acsaem.1c03920.
[16] S. Ruan, M. Shi, H. Huang, Y. Xia, J. Zhang, Y. Gan, X. Xia, X. He, W. Zhang, An innovative design of integrative polyaniline/carbon foam flexible electrode material with improved electrochemical performance, Mater. Today Chem. 29 (2023) 101435, https://doi.org/10.1016/j.mtchem.2023.101435.
[17] S. Najib, E. Erdem, Current progress achieved in novel materials for supercapacitor electrodes: mini review, Nanoscale Adv. 1 (2019) 2817–2827, https://doi.org/10.1039/C9NA00345B.
[18] Poonam, K. Sharma, A. Arora, S.K. Tripathi, Review of supercapacitors: materials and devices, J. Energy Storage 21 (2019) 801–825, https://doi.org/10.1016/j.est.2019.01.010.
[19] G.W. Shao, R. Yu, N.L. Chen, M.D. Ye, X.Y. Liu, Stretchable supercapacitors: from materials and structures to devices, Small Methods 5 (2021) 2000853, https://doi.org/10.1002/smtd.202000853.
[20] T.N. Vinuth Raj, P.A. Hoskeri, H.B. Muralidhara, C.R. Manjunatha, K.Y. Kumar, M. S. Raghu, Facile synthesis of perovskite lanthanum aluminate and its green reduced graphene oxide composite for high performance supercapacitors, J. Ele Anal. Chem. 858 (2020) 113830, https://doi.org/10.1016/j.jelechem.2020.113830.
[21] M. Wang, D. He, M. Zhu, L. Wu, Z. Wang, Z.H. Huang, H. Yang, Green fabrication of hierarchically porous carbon microtubes from biomass waste via self-activation for high-energy-density supercapacitor, J. Power Sources 560 (2023) 232703, https://doi.org/10.1016/j.jpowsour.2023.232703.
[22] T.N. Vinuth Raj, P.A. Hoskeri, H.B. Muralidhara, B.P. Prasanna, K.Y. Kumar, F. A. Alharthi, M.S. Raghu, Tantalum pentoxide functionalized nitrogen-doped reduced graphene oxide as a competent electrode material for enhanced specific capacitance in a hybrid supercapacitor device, J. Alloys Compd. 861 (2021) 158572, https://doi.org/10.1016/j.jallcom.2020.158572.
[23] X. Zhang, C. Jiang, J. Liang, W. Wu, Electrode materials and device architecture strategies for flexible supercapacitors in wearable energy storage, J. Mater. Chem. A 9 (13) (2021) 8099–8128, https://doi.org/10.1039/d0ta12299h.
[24] J. Xu, Y. He, S. Bi, M. Wang, P. Yang, D. Wu, J. Wang, F. Zhang, An olefin-linked covalent organic framework as a flexible thin-film electrode for a high-performance micro-supercapacitor, Angew. Chem. Int. Ed. 58 (35) (2019) 12065–12069, https://doi.org/10.1002/anie.201905713.
[25] A.F. Saber, S.U. Sharma, J.T. Lee, A.F.M. EL-Mahdy, S.W. Kuo, Carbazole-conjugated microporous polymers from Suzuki–Miyaura coupling for supercapacitors, Polymer (Guildf) 254 (2022) 125070–125077, https://doi.org/10.1016/j.polymer.2022.125070.
[26] B. Yan, J.J. Zheng, L. Feng, C. Du, S.J. Jian, W.S. Yang, Y.M.A. Wu, S.H. Jiang, S. J. He, W. Chen, Wood-derived biochar as thick electrodes for high-rate performance supercapacitors, Biochar 4 (2022), https://doi.org/10.1007/s42773-022-00176-9.
[27] Q. Wu, C. Jiang, S.Y. Zhang, S.T. Yu, L. Huang, Self-assembly of biomass-based hybrid hydrogel electrode for an additive-free flexible supercapacitor, J. Mater. Chem. 10 (2022) 16853–16865, https://doi.org/10.1039/d2ta03710f.
[28] M. Hong, B.C. Luo, C. Zhou, S.S. Xu, L.Y. Zhang, Z.L. Zhang, Z. Yang, N.T. Hu, Y. F. Zhang, Z. Liang, NiCoP nanoparticle-decorated carbon nanosheet arrays assembled on nickel nanowires for volumetric energy-dense supercapacitors, J. Mater. Chem. 10 (2022) 18000–18013, https://doi.org/10.1039/D2TA04307F.
[29] W.X. Hu, H.K. Fu, L. Chen, X. Wu, B. Geng, Y.L. Huang, Y.F. Xu, M. Du, G. Shan, Y. Song, Z.L. Wu, Q. Zheng, Synthesis of amorphous Nickel-Cobalt hydroxides with high areal capacitance by one-step electrodeposition using polymeric additive, Chem. Eng. J. 451 (2023) 138613, https://doi.org/10.1016/j.cej.2022.138613.
[30] Y. Li, S. Zheng, X. Liu, P. Li, L. Sun, R. Yang, S. Wang, Z. Wu, X. Bao, W.Q. Deng, Conductive microporous covalent triazine-based framework for high-performance electrochemical capacitive energy storage, Angew. Chem. Int. Ed. 130 (2018) 8124–8128, https://doi.org/10.1002/ange.201711169.
[31] P. Gao, L. Zhong, B. Han, M. He, Y. Sun, Green carbon science: keeping the pace in practice, Angew Chem. Int. Ed. Engl. 61 (2022) e202210095, https://doi.org/10.1002/anie.202210095.
[32] C.J. Chen, Y. Zhang, Y.J. Li, Y.D. Kuang, J.W. Song, W. Luo, Y.B. Wang, Y.G. Yao, G. Pastel, J. Xie, L.B. Hu, Highly conductive, lightweight, low-tortuosity carbon frameworks as ultrathick 3D current collectors, Adv. Energy Mater. 7 (2017) 1700595, https://doi.org/10.1002/aenm.201700595.
[33] A.R. Selvaraj, D. Chinnadurai, I. Cho, J.S. Bak, K. Prabakar, Bio-waste wood-derived porous activated carbon with tuned microporosity for high performance supercapacitors, J. Energy Storage 52 (2022) 104928, https://doi.org/10.1016/j.est.2022.104928.
[34] G.J. Lv, X. Dai, Y.D. Qiao, Q. Tan, Y.N. Liu, Y.Z. Chen, Functional combination of methylene blue and porous carbon mutually promotes to deliver ultrahigh rate capacitive and energy storage performance, Chem. Eng. J. 448 (2022) 137600, https://doi.org/10.1016/j.cej.2022.137660.
[35] A.M. Khattak, H. Sin, Z.A. Ghazi, X. He, B. Liang, N.A. Khan, H.R. Alanagh, A. Iqbal, L.S. Li, Z.Y. Tang, Controllable fabrication of redox-active conjugated microporous polymers on reduced graphene oxide for high performance faradaic energy storage, J. Mater. Chem. A 6 (2018) 18827–18832, https://doi.org/10.1039/C8TA07913G.
[36] Y. Zhu, P. Xu, X. Zhang, D. Wu, Emerging porous organic polymers for biomedical applications, Chem. Soc. Rev. 51 (2022) 1377–1414, https://doi.org/10.1039/D1CS00871D.
[37] A.F. Saber, K.Y. Chen, A.F.M. EL-Mahdy, S.W. Kuo, Designed azo-linked conjugated microporous polymers for CO_2 uptake and removal applications, J. Polym. Res. 28 (2021) 1–12, https://doi.org/10.1007/s10965-021-02803-8.
[38] T. Zhang, G. Xing, W. Chen, L. Chen, Porous organic polymers: a promising platform for efficient photocatalysis, Mater. Chem. Front. 4 (2020) 332–353, https://doi.org/10.1039/C9QM00633H.
[39] A.F. Saber, C.C. Chueh, M. Rashad, S.W. Kuo, A.F.M. EL-Mahdy, Thiazolyl-linked conjugated microporous polymers for enhancement adsorption and photocatalytic degradation of organic dyes from water, Mater. Today Sustain. 23 (2023) 100429, https://doi.org/10.1016/j.mtsust.2023.100429.
[40] D. Yuan, W. Lu, D. Zhao, H.C. Zhou, Highly stable porous polymer networks with exceptionally high gas uptake capacities, Adv. Mater. 23 (2011) 3723–3725, https://doi.org/10.1002/adma.201101759.
[41] S. Das, P. Heasman, T. Ben, S. Qiu, Porous organic materials: strategic design and structure–function correlation, Chem. Rev. (117) (2017) 1515–1563, https://doi.org/10.1021/acs.chemrev.6b00439.

[42] A.F. Saber, A.F.M. EL-Mahdy, (E)-1,2-Diphenylethene-based conjugated nanoporous polymers for a superior adsorptive removal of dyes from water, New J. Chem. 45 (2021) 21834–21843, https://doi.org/10.1039/D1NJ04287D.
[43] X. Guan, F. Chen, Q. Fang, S. Qiu, Design and applications of three dimensional covalent organic frameworks, Chem. Soc. Rev. 49 (2020) 1357–1384, https://doi.org/10.1039/C9CS00911F.
[44] C. Liu, Y. Jin, Z. Yu, L. Gong, H. Wang, B. Yu, W. Zhang, J. Jiang, Transformation of porous organic cages and covalent organic frameworks with efficient iodine vapor capture performance, J. Am. Chem. Soc. 144 (2022) 12390–12399, https://doi.org/10.1021/jacs.2c03959.
[45] A. Abid, S. Razzaque, I. Hussain, B. Tan, Eco-friendly phosphorus and nitrogen-rich inorganic–organic hybrid hypercross-linked porous polymers via a low-cost strategy, Macromolecules 55 (2021) 5848–5855, https://doi.org/10.1021/acs.macromol.1c00385.
[46] X. Shi, Z. Zhang, M. Wei, X. Wang, J. Wang, Y. Zhang, Y. Wang, Three-dimensional covalent organic framework membranes: synthesis by oligomer interfacial ripening and application in precise separations, Macromolecules 55 (2022) 3259–3266, https://doi.org/10.1021/acs.macromol.1c02333.
[47] C. Ru, T. Zhou, J. Zhang, X. Wu, P. Sun, P. Chen, L. Zhou, H. Zhao, J. Wu, X. Pan, Introducing secondary acceptors into conjugated polymers to improve photocatalytic hydrogen evolution, Macromolecules 54 (2021) 8839–8848, https://doi.org/10.1021/acs.macromol.1c00705.
[48] P. Zhang, Y. Yin, Z. Wang, C. Yu, Y. Zhu, D. Yan, W. Liu, Y. Mai, Porphyrin-based conjugated microporous polymer tubes: template-free synthesis and a photocatalyst for visible-light-driven thiocyanation of anilines, Macromolecules 54 (2021) 3543–3553, https://doi.org/10.1021/acs.macromol.1c00190.
[49] X. Liu, C.F. Liu, S. Xu, T. Cheng, S. Wang, W.Y. Lai, W. Huang, Porous organic polymers for high-performance supercapacitors, Chem. Soc. Rev. 51 (2022) 3181–3225, https://doi.org/10.1039/D2CS00065B.
[50] K.Y. Geng, V. Arumugam, H.J. Xu, Y.N. Gao, D.L. Jiang, Covalent organic frameworks: polymer chemistry and functional design, Prog. Polym. Sci. 108 (2020) 101288, https://doi.org/10.1016/j.progpolymsci.2020.101288.
[51] A.F. Saber, A.M. Elewa, H.H. Chou, A.F.M. EL-Mahdy, Donor-acceptor carbazole-based conjugated microporous polymers as photocatalysts for visible-light-driven H_2 and O_2 evolution from water splitting, Appl. Catal. B 316 (2022) 121624, https://doi.org/10.1016/j.apcatb.2022.121624.
[52] X. Yan, H. Liu, Y. Li, W. Chen, T. Zhang, Z. Zhao, G. Xing, L. Chen, Ultrastable covalent organic frameworks via self-polycondensation of an A2B2 monomer for heterogeneous photocatalysis, Macromolecules 52 (2019) 7977–7983, https://doi.org/10.1021/acs.macromol.9b01600.
[53] A.F. Saber, A.M. Elewa, H.H. Chou, A.F.M. EL-Mahdy, Donor to acceptor charge transfer in carbazole-based conjugated microporous polymers for enhanced visible-light-driven photocatalytic water splitting, ChemCatChem 15 (2023) e202201287, https://doi.org/10.1002/cctc.202201287.
[54] D. Li, F. Li, H. Yu, L. Guo, J. Huang, J. Li, C. Li, Nickel modified triphenylamine-based conjugated porous polymers as precatalyst for ethylene oligomerization, Inorg. Chim. Acta 544 (2022) 121228, https://doi.org/10.1016/j.ica.2022.121228.
[55] A.F. Saber, M. Ahmed, S.W. Kuo, A.F.M. EL-Mahdy, Tetraphenylcyclopentadiene-based conjugated microporous polymers for high-performance energy storage carbons, Polym. Chem. 14 (2023) 4079–4088, https://doi.org/10.1039/D3PY00671A.
[56] A.F. Saber, S.W. Kuo, A.F.M. EL-Mahdy, Microporous carbons derived from nitrogen-rich triazatruxene-based porous organic polymers for efficient cathodic supercapacitors, J. Mater. Chem. A 12 (2024) 15373–15385, https://doi.org/10.1039/D4TA01242A.
[57] S. Yuan, S. Kirklin, B. Dorney, D.J. Liu, L. Yu, Nanoporous polymers containing stereocontorted cores for hydrogen storage, Macromolecules 42 (2009) 1554–1559, https://doi.org/10.1021/ma802394x.
[58] J.P. Paraknowitsch, A. Thomas, Doping carbons beyond nitrogen: an overview of advanced heteroatom doped carbons with boron, sulphur and phosphorus for energy applications, Energy Environ. Sci. 6 (2013) 2839–2855, https://doi.org/10.1039/C3EE41444B.
[59] K.N. Wood, R. O'Hayre, S. Pylypenko, Recent progress on nitrogen/carbon structures designed for use in energy and sustainability applications, Energy Environ. Sci. 7 (2014) 1212–1249, https://doi.org/10.1039/C3EE44078H.
[60] M. Arslan, B. Kiskan, Y. Yagci, Benzoxazine-based thermosets with autonomous self-healing ability, Macromolecules 48 (2015) 1329–1334, https://doi.org/10.1021/ma5025126.
[61] R. Mahfud, T. Agag, H. Ishida, S. Shaikh, S. Qutubuddin, Synthesis and evaluation of novel anionic polymeric surfactants based on polybenzoxazines, J. Colloid Interface Sci. 407 (2013) 339–347, https://doi.org/10.1016/j.jcis.2013.06.042.
[62] S.W. Choi, J.O. Park, C. Pak, K.H. Choi, J.C. Lee, H. Chang, Design and synthesis of cross-linked copolymer membranes based on poly(benzoxazine) and polybenzimidazole and their application to an electrolyte membrane for a high-temperature PEM fuel cell, Polymers (Basel) 5 (2013) 77–111, https://doi.org/10.3390/polym5010077.
[63] S.M. Alhassan, S. Qutubuddin, D.A. Schiraldi, T. Agag, H. Ishida, Preparation and thermal properties of graphene oxide/main chain benzoxazine polymer, Eur. Polym. J. 49 (2013) 3825–3833, https://doi.org/10.1016/j.eurpolymj.2013.09.005.
[64] J. Liu, H. Ishida, Anomalous isomeric effect on the properties of bisphenol F-based benzoxazines: toward the molecular design for higher performance, Macromolecules 47 (2014) 5682–5690, https://doi.org/10.1021/ma501294y.
[65] U. Thubsuang, H. Ishida, S. Wongkasemjit, T. Chaisuwan, Improvement in the pore structure of polybenzoxazine-based carbon xerogels through a silica templating method, J. Porous Mater. 21 (2014) 401–411, https://doi.org/10.1007/s10934-014-9786-7.
[66] L. Wan, J. Wang, C. Feng, Y. Sun, K. Li, Synthesis of polybenzoxazine based nitrogen-rich porous carbons for carbon dioxide capture, Nanoscale 7 (2015) 6534–6544, https://doi.org/10.1039/C4NR07409B.
[67] O.S. Taskin, B. Kiskan, A. Aksu, N. Balkis, J. Weber, Y. Yagci, Polybenzoxazine: a powerful tool for removal of mercury salts from water, Chem. Eur. J. 20 (2014) 10953–10958, https://doi.org/10.1002/chem.201403200.
[68] S. Wang, L. Zhang, F. Han, W.C. Li, Y.Y. Xu, W.H. Qu, A.H. Lu, Diaminohexane-assisted preparation of coral-like, poly(benzoxazine)-based porous carbons for electrochemical energy storage, ACS Appl. Mater. Interfaces 6 (2014) 11101–11109, https://doi.org/10.1021/am5034796.
[69] M. Sevilla, A.B. Fuertes, Fabrication of porous carbon monoliths with a graphitic framework, Carbon N Y 56 (2013) 155–166, https://doi.org/10.1016/j.carbon.2012.12.090.
[70] S. Xu, J. He, S. Jin, B. Tan, Heteroatom-rich porous organic polymers constructed by benzoxazine linkage with high carbon dioxide adsorption affinity, J. Colloid Interface Sci. 509 (2018) 457–462, https://doi.org/10.1016/j.jcis.2017.09.009.
[71] M. Fouillaud, M. Venkatachalam, E. Girard-Valenciennes, Y. Caro, L. Dufossè, Anthraquinones and derivatives from marine-derived fungi: structural diversity and selected biological activities, Mar. Drugs 14 (2016) 64, https://doi.org/10.3390/md14040064.
[72] G. Greco, E. Turrini, E. Catanzaro, C. Fimognari, Marine anthraquinones: pharmacological and toxicological issues, Mar. Drugs 19 (2021) 272, https://doi.org/10.3390/md19050272.
[73] Q. Huang, G. Lu, H.M. Shen, M.C. Chung, C.N. Ong, Anti-cancer properties of anthraquinones from rhubarb, Med. Res. Rev. 27 (2007) 609–630, https://doi.org/10.1002/med.20094.
[74] C.P. Osman, N.H. Ismail, R. Ahmad, N. Ahmat, K. Awang, F.M. Jaafar, Anthraquinones with antiplasmodial activity from the roots of Rennellia elliptica Korth. (Rubiaceae), Molecules 15 (2010) 7218–7226, https://doi.org/10.3390/molecules15107218.
[75] D.L. Barnard, D.W. Fairbairn, K.L. O'Neill, T.L. Gage, R.W. Sidwell, Anti-human cytomegalovirus activity and toxicity of sulfonated anthraquinones and anthraquinone derivatives, Antivir. Res. 28 (1995) 317–329, https://doi.org/10.1016/0166-3542(95)00057-7.
[76] S. Mahanty, K. Rathinasamy, The natural anthraquinone dye purpurin exerts antibacterial activity by perturbing the FtsZ assembly, Bioorg. Med. Chem. 50 (2021) 116463, https://doi.org/10.1016/j.bmc.2021.116463.
[77] D. Xin, H. Li, S. Zhou, H. Zhong, W. Pu, Effects of anthraquinones on immune responses and inflammatory diseases, Molecules 27 (2022) 3831, https://doi.org/10.3390/molecules27123831.
[78] M.R. Gerhardt, L. Tong, R. Gómez-Bombarelli, Q. Chen, M.P. Marshak, C.J. Galvin, A. Aspuru-Guzik, R.G. Gordon, M.J. Aziz, Anthraquinone derivatives in aqueous flow batteries, Adv. Energy Mater. 7 (2017) 1601488, https://doi.org/10.1002/aenm.201601488.
[79] C. Zhou, X. Lu, Z. Xin, J. Liu, Y. Zhang, Hydrophobic benzoxazine-cured epoxy coatings for corrosion protection, Prog. Org. Coat. 76 (2013) 1178–1183, https://doi.org/10.1016/j.porgcoat.2013.03.013.
[80] T. Takeichi, S. Thongpradith, T. Kawauchi, Copolymers of vinyl-containing benzoxazine with vinyl monomers as precursors for high performance thermosets, Molecules 20 (2015) 6488–6503, https://doi.org/10.3390/molecules20046488.
[81] J.S.M. Lee, A.I. Cooper, Advances in conjugated microporous polymers, Chem. Rev. 120 (2020) 2171–2214, https://doi.org/10.1021/acs.chemrev.9b00399.
[82] Q. Sheng, X. Zhong, Q. Shang, Y.Y. Dong, J. Zhao, Y. Du, Y. Xie, Triazine-based conjugated microporous polymers with different linkage units for visible light–driven hydrogen evolution, Front. Chem. 10 (2022) 854018, https://doi.org/10.3389/fchem.2022.854018.
[83] M.G. Mohamed, A.M. Elewa, M.S. Li, S.W. Kuo, Construction and multifunctional of hyper-crosslinked porous organic polymers containing ferrocene unit for high-performance iodine adsorption and supercapacitor, J. Taiwan Inst. Chem. Eng. 150 (2023) 105045, https://doi.org/10.1016/j.jtice.2023.105045.
[84] L. Mei, X. Cui, Q. Duan, Y. Li, X. Lv, H.G. Wang, Metal phthalocyanine-linked conjugated microporous polymer hybridized with carbon nanotubes as a high-performance flexible electrode for supercapacitors, Int. J. Hydrogen Energy 45 (2020) 22950–22958, https://doi.org/10.1016/j.ijhydene.2020.06.208.
[85] A.M. Khattak, Z.A. Ghazi, B. Liang, N.A. Khan, A. Iqbal, L. Li, Z. Tang, A redox-active 2D covalent organic frameworks with pyridine moieties capable of faradic energy storage, J. Mater. Chem. A 4 (2016) 16312–16317, https://doi.org/10.1039/C6TA05784E.
[86] M.M. Samy, M.G. Mohamed, A.F.M. EL-Mahdy, T.H. Mansoure, K.C.W. Wu, S. W. Kuo, High-performance supercapacitor electrodes prepared from dispersions of tetrabenzonaphthalene-based conjugated microporous polymers and carbon nanotubes, ACS Appl. Mater. Interfaces 13 (2021) 51906–51916, https://doi.org/10.1021/acsami.1c05720.
[87] M. Sethi, U.S. Shenoy, D.K. Bhat, A porous graphene–$NiFe2O_4$ nanocomposite with high electrochemical performance and high cycling stability for energy storage applications, Nanoscale Adv. 2 (2020) 4229–4241, https://doi.org/10.1039/D0NA00440E.
[88] T. Brousse, D. Belanger, J.W. Long, To be or not to be pseudocapacitive? J. Electrochem. Soc. 162 (2015) A5185–A5189, https://doi.org/10.1149/2.0201505jes.
[89] P. Simon, Y. Gogotsi, B. Dunn, Where do batteries end and supercapacitors begin? Science 343 (2014) 1210–1211, https://doi.org/10.1126/science.1249625.

[90] Q. Li, W. Lu, Z. Li, J. Ning, Y. Zhong, Y. Hu, Hierarchical $MoS_2/NiCo_2S_4$@C urchin like hollow microspheres for asymmetric supercapacitors, Chem. Eng. J. 380 (2020) 122544, https://doi.org/10.1016/j.cej.2019.122544.
[91] W. Lu, J. Shen, P. Zhang, Y. Zhong, Y. Hu, X.W. Lou, Construction of CoO/Co-Cu-S hierarchical tubular heterostructures for hybrid supercapacitors, Angew. Chem. Int. Ed. 58 (2019) 15441–15447, https://doi.org/10.1002/anie.201907516.
[92] E. Lim, C. Jo, H. Kim, M.H. Kim, Y. Mun, J. Chun, Y. Ye, J. Hwang, K.S. Ha, K. C. Roh, K. Kang, S. Yoon, J. Lee, Facile Synthesis of Nb_2O_5@carbon core-shell nanocrystals with controlled crystalline structure for high-power anodes in hybrid supercapacitors, ACS Nano 9 (2015) 7497–7505, https://doi.org/10.1021/acsnano.5b02601.
[93] B. Zahiri, R.M. Felix, A. Hill, C.H. Kung, T. Sharma, J.D. Real, W. Mérida, Through-plane wettability tuning of fibrous carbon layers via O_2 plasma treatment for enhanced water management, Appl. Surf. Sci. 458 (2018) 32–42, https://doi.org/10.1016/j.apsusc.2018.07.005.
[94] J. Lee, G.H. An, Surface-engineered flexible fibrous supercapacitor electrode for improved electrochemical performance, Appl. Surf. Sci. 539 (2021) 148290, https://doi.org/10.1016/j.apsusc.2020.148290.
[95] M. Mirzaeian, A.A. Ogwu, H.F. Jirandehi, S. Aidarova, Z. Ospanova, N. Tsendzughul, Surface characteristics of silver oxide thin film electrodes for supercapacitor applications, Colloids Surf. A Physicochem. Eng. Asp 519 (2017) 223–230, https://doi.org/10.1016/j.colsurfa.2016.04.026.
[96] J. Liu, D. Xuan, Z. Lu, Z. Wang, Q. Liu, S. Li, D. Wang, Y. Ye, D. Wang, Z. Zheng, A novel perspective on interfacial interactions between polypyrrole and carbon materials for improving performance of supercapacitors, Appl. Surf. Sci. 573 (2022) 151626, https://doi.org/10.1016/j.apsusc.2021.151626.